Applied Physics Letters

All-epitaxial guided-mode resonance mid-wave infrared detectors

Cite as: Appl. Phys. Lett. **118**, 201102 (2021); https://doi.org/10.1063/5.0047534
Submitted: 14 February 2021 . Accepted: 01 May 2021 . Published Online: 17 May 2021

A. Kamboj, L. Nordin, P. Petluru, A. J. Muhowski, D. N. Woolf, and D. Wasserman

AIP Publishing

Applied Physics Letters ARTICLE scitation.org/journal/apl

All-epitaxial guided-mode resonance mid-wave infrared detectors

Cite as: Appl. Phys. Lett. **118**, 201102 (2021); doi: 10.1063/5.0047534
Submitted: 14 February 2021 · Accepted: 1 May 2021 ·
Published Online: 17 May 2021

A. Kamboj,[1] L. Nordin,[1] P. Petluru,[1] A. J. Muhowski,[1] D. N. Woolf,[2] and D. Wasserman[1,a)]

AFFILIATIONS

[1]Electrical and Computer Engineering, University of Texas at Austin, Austin, Texas 78758, USA
[2]Physical Sciences Inc., Andover, Massachusetts 01810, USA

[a)]Author to whom correspondence should be addressed: dw@utexas.edu

ABSTRACT

We demonstrate all-epitaxial guided-mode resonance mid-wave infrared (MWIR) type-II superlattice nBn photodetectors. Our detectors consist of a high-index absorber/waveguide layer grown above a heavily doped (n^{++}), and thus, low-index, semiconductor layer, and below a high-index and wide-bandgap grating-patterned layer. Polarization- and angle-dependent detector response is measured experimentally and simulated numerically, showing strongly enhanced absorption, compared to unpatterned detectors, at wavelengths associated with coupling to guided-mode resonances in our fabricated detectors. The detectors show high operating temperature (T = 200 K) external quantum efficiencies over 50% for TE-polarized light with absorber thickness of only 250 nm ($\sim\lambda_o/20$). We calculate T = 200 K estimated specific detectivity for our detectors, on resonance, of $\sim 4 \times 10^{10}$ cm Hz$^{1/2}$ W^{-1}, comparable with state-of-the-art MWIR detectors. The presented results offer an approach to monolithic, all-epitaxial integration of IR detector architectures with resonant optical cavities for enhanced detector response across the mid-wave infrared.

The mid-infrared (mid-IR) portion of the electromagnetic spectrum ($\lambda \sim 3 - 30\,\mu$m) is a wavelength range of significant importance for fundamental scientific investigation and a range of technological applications. Within the mid-IR, the mid-wave infrared (MWIR, $\lambda = 3 - 5\,\mu$m) is of particular importance for gas sensing, free space communication, and thermal imaging of high temperature objects, due to its overlap with the shortest wavelength atmospheric transmission window in the mid-IR, as well as its position as the spectral home for the peak thermal emission from objects with temperatures $\sim 580 - 970$ K.[1–3] All of the above applications require efficient, and often high speed, detectors. Though advances in micro-bolometer technology have made thermal imaging arrays significantly more sensitive and cost-efficient, such detectors do not offer the dynamic range, responsivity, or response speeds necessary for many IR sensing, communication, or imaging applications.[4] For such applications, semiconductor-based photodetectors are required, traditionally photodiodes fabricated in the mercury–cadmium–telluride (MCT) or InSb material systems.[4,5]

Recently, there has been significant interest in a class of mid-IR detector materials, type-II superlattices (T2SLs), consisting of nanoscale layers of alternating semiconductor alloys (usually in the 6.1 Å lattice constant family) with type-II band offsets.[6–9] The periodic nature of the superlattice, combined with layer thicknesses on the order of electron wavelengths, results in superlattice minibands whose energies are controlled by both alloy composition and layer thicknesses. In this way, T2SL-based detectors offer significant flexibility in absorber design (with cutoff wavelengths ranging from $\lambda_{co} \sim 3 - 30\,\mu$m) and detector architecture (not only traditional photodiodes, but also bariode architectures).[10–14] T2SL absorbers have been shown to have lower Auger recombination rates, and have been predicted to have lower dark currents, than bulk semiconductor absorbers with the same λ_{co}.[15,16] The implementation of the bariode design architectures has led to further improvement of dark current characteristics in these T2SL-based detectors resulting from the suppression of Shockley–Read–Hall (SRH) recombination, paving the way for higher temperature operation.[14,17] Offsetting these benefits, T2SL absorption coefficients are typically smaller than those of comparable bulk semiconductor detectors, resulting in a trade-off between the design flexibility and improved dark current predicted for T2SLs, and the decreased responsivity associated with lower absorption coefficients.[18] Growing thicker detectors can offset some of the decrease in detector absorption, but such an approach has limited returns, a result of the finite diffusion length for minority carriers and the dependence of dark current on detector thickness.[17,19,20]

A potential approach to address the weaker absorption in T2SL-based detectors is the integration of the absorber into resonant optical structures. Such cavities can take the form of distributed Bragg reflectors, metal surface gratings, or metal–insulator–metal structures.[21–24] At mid-IR wavelengths, the former requires numerous thick, epitaxially grown layers while the latter requires multiple metallization and patterning steps, as well as substrate removal, which significantly increases the fabrication complexity of the detector devices. Recently, the monolithic integration of long wave infrared (LWIR, $\lambda = 8$–$13\,\mu$m) T2SL detectors with heavily doped n^{++} semiconductor ground planes has been proposed[25] and demonstrated[26] to offer significant absorption enhancement in thin, all-epitaxial, detector structures. The permittivity of these heavily doped semiconductors follows the Drude model for free carrier response, and thus, in the LWIR, can behave as plasmonic materials.[27–29] However, the doping concentration required to achieve negative permittivity in n^{++} III–V semiconductors, across the MWIR, is much higher than what has been demonstrated experimentally, precluding all-epitaxial plasmonic device architectures in the MWIR. Such high doping can, nonetheless, provide a large index contrast between the n^{++} semiconductor and the overgrown T2SL, thus forming a dielectric waveguide for strong MWIR mode confinement.

The control of semiconductor permittivity by doping, thus, opens the door, even in the MWIR, to a number of optical architectures for improved absorption in T2SL (or other MWIR absorber) materials. In particular, the ability to design and grow all-epitaxial dielectric waveguide structures offers the opportunity for the integration of MWIR detectors into guided-mode resonance (GMR) structures.[30–32] The GMR phenomenon is observed in waveguides consisting of a high-index dielectric core (patterned with a grating), sandwiched between two lower index layers. While the grating couples incident light into the dielectric waveguide modes, it also allows outcoupling from these modes to free space. At resonance, there is destructive interference between the transmitted (reflected) incident light, and the light which couples to (and then outcouples from) a waveguide mode, resulting in a transmission (reflection) null, and reflection (transmission) maximum, with extremely narrow bandwidth. The spectral features associated with these resonances can be tuned by control of the grating and waveguide dimensions, as well as the angle and polarization of the incident light. GMR structures are of particular appeal for optical filtering applications, offering strong spectral features in structures having thicknesses on the order of a wavelength or less (compared to much thicker optical interference filters).[33] In addition, there has been significant effort to demonstrate the integration of optoelectronic devices in GMR architectures for enhanced solar cell efficiency and laser operation.[34,35]

In this work, we propose and demonstrate an all-epitaxial GMR structure with a MWIR T2SL nBn detector monolithically integrated into the resonant waveguide [Fig. 1(a)]. We leverage the ability to control our semiconductor permittivity during epitaxial growth, using doping concentration, to grow dielectric waveguide structures with high-index contrast between the core (our MWIR detector) and the cladding (n^{++} semiconductor and air) layers [Figs. 1(b) and 1(c)]. We model, grow, fabricate, and characterize the GMR photodetectors and report spectrally selective absorption enhancement (>10×) with resonant absorption tunable across the MWIR. We demonstrate on-resonance TE-polarized external quantum efficiencies (EQE) in excess of 50% from our detectors, with sub-wavelength thickness absorbers (250 nm, or $\sim\lambda_o/20$). The devices' polarization-, temperature-, and angle-dependent response is measured and compared to rigorous coupled-wave simulations with excellent agreement. While the results presented are for a single, surface-illuminated, detector element, the demonstrated architecture is also compatible with substrate-illuminated, focal plane array (FPA) configurations, with appropriate adjustments to device geometry and layer thicknesses.

Our detector structures are designed using rigorous coupled-wave analysis (RCWA),[36] which provides the reflection (R), transmission (T), and field profiles in our structures as a function of wavelength, incident angle and polarization. In our model, light is incident upon the devices in the xz plane with the GMR 1D grating periodicity in x. For this orientation, we denote s-polarized incident light (electric field E_y parallel to the sample surface) as "TE-polarized" and p-polarized incident light (magnetic field H_y parallel to the sample surface) as "TM-polarized," as shown in Fig. 2(a). The n^{++} layer is modeled as a Drude metal with plasma wavelength $\lambda_p = 6\,\mu$m and scattering rate $\gamma = 1.5 \times 10^{13}$ rad s^{-1}, extracted by fitting reflection

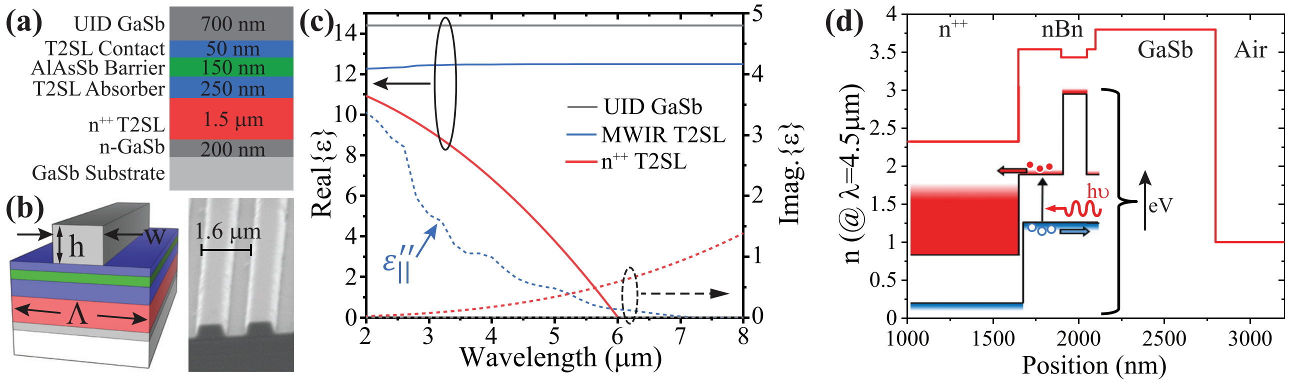

FIG. 1. (a) Layer stack of as-grown GMR detector structure. (b) Schematic of one period of fabricated GMR detector with scanning electron micrograph of detector cross section. (c) Wavelength-dependent complex permittivity for GMR detector constituent materials: GaSb (gray), MWIR T2SL (blue) and n^{++} T2SL modeled as a Drude metal (red). The imaginary component of the MWIR T2SL is $\varepsilon''_{||}$, as in our model we set $\varepsilon''_{zz} = 0$. (d) Refractive index of the detector layer stack at wavelength $\lambda = 4.5\,\mu$m. Inset shows schematic of GMR detector band structure with electron (red) and hole (blue) minibands.

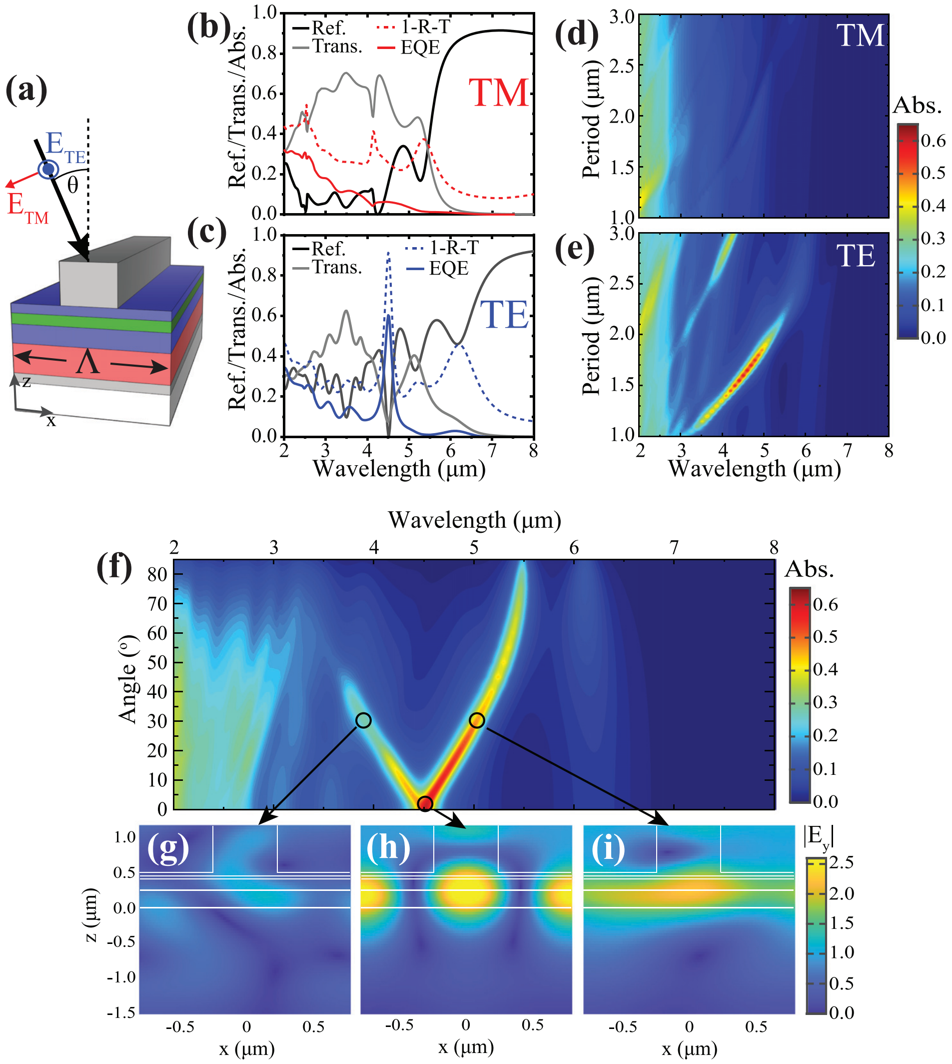

FIG. 2. (a) Schematic of GMR detector indicating incident angle and polarization. Normal-incidence transmission (gray), reflection (black), simulated EQE (color), and total absorption ($1 - R - T$, dashed color) for (b) TM- (red) and (c) TE- (blue) polarized light. EQE contour plots for (d) TM- and (e) TE-polarized normal-incidence light as a function of grating period (assuming ridge width $w = 0.3\Lambda$). (f) TE-polarized angle-dependent simulated EQE spectra for GMR detector with $\Lambda = 1.6$ and $w = 0.48\,\mu$m. Field profiles $|E_y|$ for TE-polarized resonant absorption features (g) $\lambda = 3.9\,\mu$m at $\theta = 30°$, (h) $\lambda = 4.5\,\mu$m at $\theta = 0°$, and (i) $\lambda = 5.02\,\mu$m at $\theta = 30°$. Profile of the GMR detector cross section is shown in white over each field plot.

data of calibration samples consisting only of highly doped material. The T2SL absorber and barrier layers are modeled as having constant real permittivity (ε') calculated from the weighted average of their constituent materials. We use an anisotropic imaginary permittivity (ε'') in our model of the T2SL absorber to mimic, to first order, the absorption selection rules in T2SL materials;[37] thus $\varepsilon''_{xx,yy} = \varepsilon''_{||}$ and $\varepsilon''_{zz} = 0$, where $\varepsilon''_{||}$ [the blue dashed line in Fig. 1(c)] is extracted by fitting to the experimentally measured responsivity of an unpatterned detector device. As can be seen in Fig. 1(d), the high-index contrast required to sustain the guided modes is achieved by sandwiching the high-index T2SL/GaSb between the n^{++} InAs/InAsSb and air. The 1D GaSb grating provides a grating momentum allowing incident light labeled as TE- (TM-) polarized to couple to TE (TM) modes propagating in the *x*-direction (see the supplementary material for field plots). Due to the T2SL selection rules ($\varepsilon''_{zz} = 0$), absorption in the TM modes will be weak (as the electric field is primarily in the z-direction).

Figure 1(c) shows the real and imaginary permittivity spectra of the different layers in our epitaxial stack. Using the simulated field profiles, we can extract the absorption in the detector absorber region,[25] which is effectively equivalent to EQE, as the absorber region is quite thin, particularly in comparison to the typical diffusion length of Ga-free T2SLs.[38] We thus refer to simulated absorption in the detector absorber region as the "modeled EQE" for the remainder of this work. Figures 2(b) and 2(c) show the simulated polarization-dependent *R*, *T* EQE, and total absorption ($A = 1 - R - T$) for normally incident light on a $\Lambda = 1.6\,\mu$m, $w = 0.3\Lambda$ GMR detector structure (corresponding to the geometry of our fabricated $\Lambda = 1.6\,\mu$m detector). A clear resonant absorption feature is observed at $\lambda = 4.5\,\mu$m, for TE-polarized light, corresponding to the structure's guided-mode resonance. The resonant coupling wavelength can be tuned across much of the MWIR by varying the grating period [Fig. 2(e)], or by changing the incident angle [Fig. 2(f)]. Representative electric field profiles for resonant absorption at $\theta = 0°$ and $\theta = 30°$ are shown in Figs. 2(g)–2(i), demonstrating the guided-mode nature of the resonances. Our detector structures were designed with the goal of strong (*EQE* > 50% on resonance) and spectrally selective response in the MWIR, from ultra-thin absorber layers (to minimize dark current). Additional optimization, or tuning of the device's optical and electronic properties, could certainly be achieved by further exploration of the device geometry and electronic design parameter space.

The MWIR GMR detectors were grown by molecular beam epitaxy (MBE) in a Varian Gen II system with valved cracker sources for arsenic and antimony and effusion sources for gallium, indium, aluminum, and silicon. Figure 1(a) shows the epitaxial layer stack of our detectors, which are grown on a lightly n-doped GaSb substrate. Growth begins with an n-doped GaSb buffer followed by 1.5 μm of n^{++} InAs/InAs$_{0.5}$Sb$_{0.5}$ T2SL, which serves as the low-index bottom cladding layer of the dielectric waveguide. Note that the n^{++} T2SL does not contribute to the detector photoresponse, a result of the Burstein–Moss shift in the absorption band edge (state-filling) and the negligible minority carrier lifetime in degenerately doped semiconductor materials. Following the n^{++} layer, we grow the MWIR T2SL nBn detector structure which, from the bottom up, consists of a 250 nm T2SL absorber layer, a 150 nm AlAsSb barrier, and a 50 nm n-type T2SL contact. The T2SL absorber and contact use the same InAs/InAs$_{0.5}$Sb$_{0.5}$ (19.8 ML/4.2 ML) superlattice as the n^{++} bottom cladding, with the only difference being the doping concentration. Above the nBn structure, we grow 700 nm of unintentionally doped (UID) GaSb (lightly p-doped) which serves as the high-index material for our grating.

Detector devices are fabricated by first depositing metal contacts (Ti/Pt/Au) on the top GaSb layer using a standard UV-lithography, metallization, and lift-off process. Gratings ($\Lambda = 1.6,\ 2\ \mu$m) are then fabricated in the GaSb layer using a lithographically defined SiN$_x$ etch mask and a reactive-ion etch (RIE) process (detectors left unpatterned serve as control samples). Finally, devices were electrically isolated with a mesa etch through the barrier layer, and bottom contact made to the backside of the wafer. Figure 1(b) shows a scanning electron micrograph of a representative detector device with period $\Lambda = 1.6\ \mu$m. The mesa area spans $500 \times 700\ \mu m^2$ with grating area $450 \times 450\ \mu m^2$. The polarization-dependent spectral response of the detectors was measured with a Bruker V80v Fourier-transform infrared (FTIR) spectrometer, for incident angles from 0° to 40°, and normalized to the spectra obtained from a pyroelectric detector with a spectrally flat response. Polarization-dependent detector responsivity is determined by measuring the detector signal from a calibrated blackbody source filtered by a 3.6 μm bandpass filter.[39]

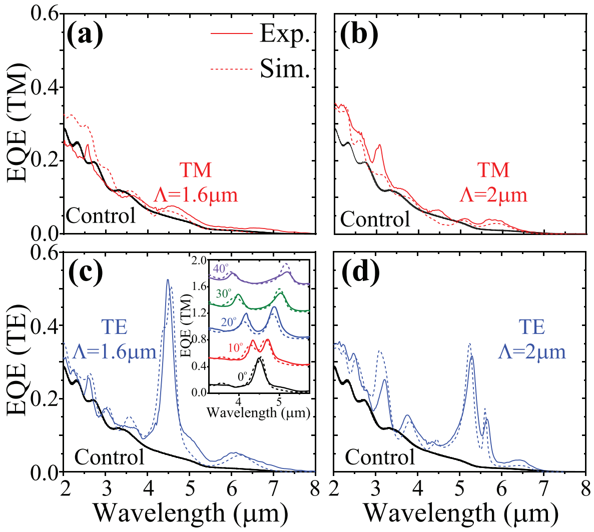

FIG. 3. Normal incidence simulated (dashed) and $T = 200$ K experimental (solid) polarization-dependent EQE of nBn MWIR GMR detectors with (a) $\Lambda = 1.6\ \mu$m (TM-polarized), (b) $\Lambda = 2\ \mu$m (TM-polarized), (c) $\Lambda = 1.6\ \mu$m (TE-polarized), and (d) $\Lambda = 2\ \mu$m (TE-polarized). Inset in (c) shows simulated (dashed) and $T = 200$ K experimental angle-dependent TE-polarized EQE for the $\Lambda = 1.6\ \mu$m detector with individual line plots offset by 0.4 for ease of viewing.

Figure 3 shows the experimental EQE for TM- and TE-polarized normal incidence light for the $\Lambda = 1.6\ \mu$m ($w = 0.48\ \mu$m) and $\Lambda = 2\ \mu$m ($w = 1\ \mu$m) GMR detectors. Our polarization-specific EQE thus provides the measure of the device quantum efficiency for purely TE (or TM) polarized light. All spectra are compared to the (polarization-independent) EQE of the unpatterned control sample, as well as the RCWA-simulated polarization-dependent EQE (modeled with an incident angular spread of ±7° to account for the focused beam of the experimental setup). Our RCWA simulations model an infinite periodic structure, which is a reasonable approximation of our uniformly grating-patterned single element detector which comprises $\sim$225 − 280 grating periods, depending on the grating dimensions. No substantive TM-polarized resonances are observed in Figs. 3(a) and 3(b), matching our predicted RCWA-calculated TM-polarized absorption in Fig. 2(d). The TE-polarized data, on the other hand, shows a strong, resonant absorption enhancement for both devices. For the $\Lambda = 1.6\ \mu$m device [Fig. 3(c)], EQE of 52.5% is observed (from the 250 nm thick absorber) at a resonant wavelength $\lambda = 4.5\ \mu$m. At this same wavelength, the control sample EQE is $\sim$4.7%, resulting in over an order of magnitude on-resonance enhancement of EQE (11×). The $\Lambda = 2\ \mu$m sample also showed a strongly enhanced EQE of $\sim$32% [Fig. 3(d)], at $\lambda = 5.3\ \mu$m, with an even stronger enhancement over the control ($\sim$17×), due to the weaker T2SL absorption at the longer wavelength resonance of the $\Lambda = 2\ \mu$m device. The inset in Fig. 3(c) shows the angle-dependent experimental and simulated TE-polarized EQE for the $\Lambda = 1.6\ \mu$m detector. A clear splitting of the absorption features is observed with increasing incident angle, as expected from our simulations in Fig. 2. For all devices, polarizations, and incident angles, our simulated EQE shows excellent agreement with our experimental results.

The MWIR GMR detectors show significant resonant enhancement, and spectral selectivity, of detector response. Engineering this strong enhancement requires a series of trade-offs, largely a result of the strongly dispersive permittivity of both the T2SL and n^{++} semiconductor materials. As can be seen in Fig. 2(f), for non-normal incidence angles, the shorter wavelength resonances show significantly weaker enhancement than their longer wavelength counterparts. This effect is primarily a result of the weaker dielectric confinement provided by the n^{++} bottom cladding layer at shorter wavelengths [seen clearly in Figs. 2(g) and 2(i)]. Fortunately, the all-epitaxial material system employed offers significant design flexibility. The T2SL absorption coefficient can be tuned across much of the MWIR by adjusting the constituent materials and/or the superlattice layer thicknesses. Similarly, control of doping concentration in the bottom cladding layer allows for control of the layer permittivity (bounded by the doping limits of the n^{++} semiconductor[28]). The ability to engineer both the semiconductor absorber material (and detector architecture) and the surrounding optical environment during epitaxial growth provides a welcome ability to control and balance the waveguiding properties of the optical structure and the detector performance.

Ultimately, detector performance is not measured solely by the device EQE; we must also take detector noise into consideration, in order to extract the detector's specific detectivity, D^* (the figure of merit allowing comparison of different detector materials, architectures, and operating wavelengths). A primary driver for the demonstration of thin IR detector architectures is the potential for significant reduction in the dark current, which for a diffusion-limited detector scales linearly with the detector thickness. Figure 4(a) shows experimental temperature-dependent dark currents for the $\Lambda = 1.6\,\mu$m GMR detector device, and Fig. 4(b) shows the temperature-dependent device dark current (black squares) at the operating bias (-0.78 V). We observe rather large device turn-on voltages (~ -0.5 V), which we attribute to a combination of hole collection through the top GaSb/T2SL interface, and a potential valence band offset between our AlAsSb barrier and MWIR T2SL (which has been observed in previous work on ultra-thin T2SL detectors[23]). In addition, we do not observe the strong dark current saturation which, in traditional nBn T2SL detectors, indicates diffusion-limited dark current operation. Future work will endeavor to understand (and mitigate) both the large turn-on voltage and weak dark current saturation observed in our devices.

The grating/waveguide structure surrounding our thin absorber makes a straightforward measurement of detector cutoff from absorption measurements difficult, as absorption is modulated by cavity/interference effects. However, $T = 200$ K photoluminescence (PL) spectra of our material, as-grown and with the GaSb layer etched off, suggests a cutoff wavelength for our detectors between 7 and 7.5 μm (see the supplementary material). Given the non-negligible detector response observed experimentally between $\lambda = 6 - 7\,\mu$m, the T2SL absorption coefficient extracted from the control sample responsivity, and our PL data, a cutoff wavelength close to $\lambda_{co} = 7\,\mu$m is realistic (even conservative) for our materials. In Fig. 4(b), we compare our device dark current to the temperature-dependent Rule07 plots (the heuristic predicted limit for infrared HgCdTe detector dark current as a function of cutoff wavelength and temperature[40]) for three different cutoff wavelengths ($\lambda_{co} = 6.5, 7$, and $7.5\,\mu$m), in order to account for the uncertainty in λ_{co}. At our operating temperature of $T = 200$ K, our detector beats Rule07 for all of the above cutoff wavelengths. For $\lambda_{co} = 7\,\mu$m, our experimentally measured dark current is over an order of magnitude less than the Rule07 limit, in line with the expected decrease in the dark current resulting from the approximate order of magnitude reduction in absorber layer thickness (compared to typical MWIR T2SL detectors) achieved in our detectors.

On-resonance, TE-polarized estimated specific detectivity for the $\Lambda = 1.6\,\mu$m detector with 300 K background is plotted in Fig. 4(c), as a function of applied bias, using the expression inset in Fig. 4(c). Though peak estimated detectivity (4.49×10^{10} cm Hz$^{1/2}$ W^{-1}) occurs at a bias of $V = -0.43$ V, detector responsivity here is weak and, thus, not particularly indicative of the potential operating conditions for the device. Instead, we indicate estimated D^* for voltages associated with 90% ($V = -0.51$ V) and 100% ($V = -0.78$ V) of the detector's peak response. For these applied biases, we nonetheless observe estimated D^*'s (4.46×10^{10} and 4.09×10^{10} cm Hz$^{1/2}$ W^{-1}, respectively) competitive with state-of-the-art MWIR detectors.[41,42] Additional improvements to detector performance could be achieved by further optimization of the device geometry, or by introducing alternative T2SL designs with stronger absorption coefficients but degraded vertical mobility (which is less important for ultra-thin detectors).

We have demonstrated an all-epitaxial guided-mode resonator with an integrated type-II superlattice nBn detector architecture for enhanced absorption in the MWIR. The low index achieved by heavily doping the cladding layer upon which our detector is grown allows our device to support a guided mode in our ultra-thin (250 nm $\ll \lambda_o$) absorber layer. We report strong modulation of the response spectra of fabricated detectors, and a $>10\times$ enhancement in EQE on resonance, compared to control samples. In our $\Lambda = 1.6\,\mu$m device, we achieve over 50% EQE, on resonance ($\lambda = 4.5\,\mu$m). Our devices beat the Rule07 heuristic for IR detector dark current and show estimated D^* over 4×10^{10} cm Hz$^{1/2}$ W^{-1}. The significant flexibility in the design of the detector's optical (by doping concentration) and electronic (by T2SL design) properties, afforded by the epitaxial growth of our GMR detectors, as well as the tuning of device operation offered by post-growth grating fabrication, opens the door to a class of detectors capable of strong spectral and polarization selectivity, on-resonance absorption, and detector response, while also showing high

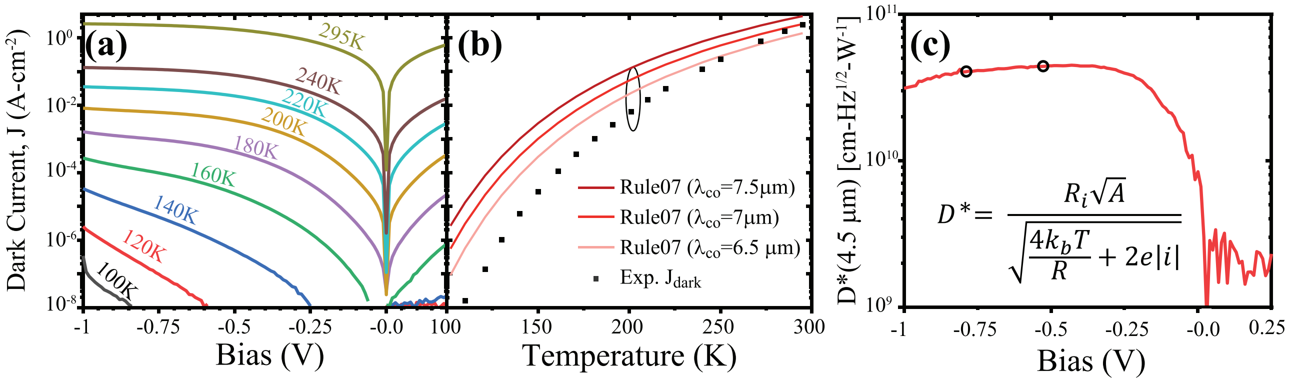

FIG. 4. (a) Temperature-dependent dark current for $\Lambda = 1.6\,\mu$m detector. (b) Rule07 ($\lambda_{co} = 6.5$, 7, and $7.5\,\mu$m, red lines) and experimentally measured (operating bias -0.78 V, black squares) temperature-dependent dark currents. (c) $T = 200$ K TE-polarized estimated D^*, calculated from experimentally measured responsivity with 300 K background. Black circles indicate operational bias for peak (-0.78 V) and 90% of peak (-0.51 V) responsivity.

estimated D* and low-noise operation, for a range of infrared-sensing and imaging applications.

See the supplementary material for more information on simulated field profiles, reflectivity, and photoluminescence characterization of the detector.

This material was based upon work supported by the United States Army under Prime Contract No. W909MY-20-P-0010. Any opinions, findings, and conclusions or recommendations expressed in this material are those of the author(s) and do not necessarily reflect the views of the U.S. Army. The authors gratefully acknowledge support from the National Science Foundation (No. ECCS-1926187 and MRSEC Program No. DMR-1720595). Part of the work was done at the University of Texas Microelectronics Research Center (The Texas Nanofabrication Facility), a member of the National Nanotechnology Coordinated Infrastructure (NNCI), supported by the National Science Foundation (No. ECCS-2025227).

DATA AVAILABILITY

The data that support the findings of this study are available from the corresponding author upon reasonable request.

REFERENCES

[1] P. Werle, F. Slemr, K. Maurer, R. Kormann, R. Mücke, and B. Jänker, Opt. Lasers Eng. **37**, 101–114 (2002).
[2] A. Soibel, M. W. Wright, W. H. Farr, S. A. Keo, C. J. Hill, R. Q. Yang, and H. C. Liu, IEEE Photonics Technol. Lett. **22**, 121–123 (2010).
[3] K. Krapels, R. G. Driggers, D. Deaver, S. K. Moyer, and J. Palmer, Appl. Opt. **46**, 7345–7353 (2007).
[4] A. Rogalski, *Infrared Detectors*, 2nd ed. (CRC Press, Boca Raton, FL, 2011).
[5] A. Rogalski, Rep. Prog. Phys. **68**, 2267–2336 (2005).
[6] D. L. Smith and C. Mailhiot, J. Appl. Phys. **62**, 2545–2548 (1987).
[7] C. Mailhiot and D. L. Smith, J. Vac. Sci. Technol. A **7**, 445–449 (1989).
[8] R. H. Miles, D. H. Chow, J. N. Schulman, and T. C. McGill, Appl. Phys. Lett. **57**, 801–803 (1990).
[9] A. Haddadi, G. Chen, R. Chevallier, A. M. Hoang, and M. Razeghi, Appl. Phys. Lett. **105**, 121104 (2014).
[10] H. Mohseni, M. Razeghi, G. J. Brown, and Y. S. Park, Appl. Phys. Lett. **78**, 2107–2109 (2001).
[11] Y. Wei, A. Gin, M. Razeghi, and G. J. Brown, Appl. Phys. Lett. **81**, 3675–3677 (2002).
[12] J. B. Rodriguez, E. Plis, G. Bishop, Y. D. Sharma, H. Kim, L. R. Dawson, and S. Krishna, Appl. Phys. Lett. **91**, 043514 (2007).
[13] H. S. Kim, E. Plis, J. B. Rodriguez, G. D. Bishop, Y. D. Sharma, L. R. Dawson, S. Krishna, J. Bundas, R. Cook, D. Burrows, R. Dennis, K. Patnaude, A. Reisinger, and M. Sundaram, Appl. Phys. Lett. **92**, 183502 (2008).
[14] D. Z.-Y. Ting, C. J. Hill, A. Soibel, S. A. Keo, J. M. Mumolo, J. Nguyen, and S. D. Gunapala, Appl. Phys. Lett. **95**, 023508 (2009).
[15] C. H. Grein, M. E. Flatté, J. T. Olesberg, S. A. Anson, L. Zhang, and T. F. Boggess, J. Appl. Phys. **92**, 7311–7316 (2002).
[16] B. V. Olson, C. H. Grein, J. K. Kim, E. A. Kadlec, J. F. Klem, S. D. Hawkins, and E. A. Shaner, Appl. Phys. Lett. **107**, 261104 (2015).
[17] S. Maimon and G. W. Wicks, Appl. Phys. Lett. **89**, 151109 (2006).
[18] A. Rogalski, P. Martyniuk, and M. Kopytko, Prog. Quantum Electron. **68**, 100228 (2019).
[19] D. R. Rhiger, J. Electron. Mater. **40**, 1815–1822 (2011).
[20] B. V. Olson, J. K. Kim, E. A. Kadlec, J. F. Klem, S. D. Hawkins, D. Leonhardt, W. T. Coon, T. R. Fortune, M. A. Cavaliere, A. Tauke-Pedretti, and E. A. Shaner, Appl. Phys. Lett. **107**, 183504 (2015).
[21] J. A. Nolde, M. Kim, C. S. Kim, E. M. Jackson, C. T. Ellis, J. Abell, O. J. Glembocki, C. L. Canedy, J. G. Tischler, I. Vurgaftman, J. R. Meyer, and E. H. Aifer, Appl. Phys. Lett. **106**, 261109 (2015).
[22] M. D. Goldflam, E. A. Kadlec, B. V. Olson, J. F. Klem, S. D. Hawkins, S. Parameswaran, W. T. Coon, G. A. Keeler, T. R. Fortune, A. Tauke-Pedretti, J. R. Wendt, E. A. Shaner, P. S. Davids, J. K. Kim, and D. W. Peters, Appl. Phys. Lett. **109**, 251103 (2016).
[23] V. Letka, A. Bainbridge, A. P. Craig, F. Al-Saymari, and A. R. J. Marshall, Opt. Express **27**, 23970–23980 (2019).
[24] C. L. Canedy, W. W. Bewley, C. D. Merritt, C. S. Kim, M. Kim, M. V. Warren, E. M. Jackson, J. A. Nolde, C. A. Affouda, E. H. Aifer, I. Vurgaftman, and J. R. Meyer, Opt. Express **27**, 3771–3781 (2019).
[25] S. Wang, N. Yoon, A. Kamboj, P. Petluru, W. Zheng, and D. Wasserman, Appl. Phys. Lett. **112**, 091104 (2018).
[26] L. Nordin, A. Kamboj, P. Petluru, E. Shaner, and D. Wasserman, ACS Photonics **7**, 1950–1956 (2020).
[27] S. Law, D. C. Adams, A. M. Taylor, and D. Wasserman, Opt. Express **20**, 12155–12165 (2012).
[28] S. Law, L. Yu, and D. Wasserman, J. Vac. Sci. Technol. B **31**, 03C121 (2013).
[29] W. Streyer, S. Law, G. Rooney, T. Jacobs, and D. Wasserman, Opt. Express **21**, 9113–9122 (2013).
[30] S. S. Wang, R. Magnusson, J. S. Bagby, and M. G. Moharam, J. Opt. Soc. Am. A **7**, 1470–1474 (1990).
[31] S. S. Wang and R. Magnusson, Appl. Opt. **32**, 2606–2613 (1993).
[32] R. Magnusson and S. S. Wang, Appl. Opt. **34**, 8106–8109 (1995).
[33] Y. Zhong, Z. Goldenfeld, K. Li, W. Streyer, L. Yu, L. Nordin, N. Murphy, and D. Wasserman, Opt. Lett. **42**, 223–226 (2017).
[34] T. Khaleque, J. Yoon, W. Wu, and R. Magnusson, *Renewable Energy and the Environment* (Optical Society of America), p. PWD3.
[35] T. Kondo, S. Ura, and R. Magnusson, J. Opt. Soc. Am. A **32**, 1454–1458 (2015).
[36] V. A. Podolskiy's Research Group, see http://faculty.uml.edu/vpodolskiy/codes/index.html for "An Implementation of Rigorous Coupled Wave Analysis."
[37] N. F. Johnson, H. Ehrenreich, P. M. Hui, and P. M. Young, Phys. Rev. B **41**, 3655–3669 (1990).
[38] D. Zuo, R. Liu, D. Wasserman, J. Mabon, Z.-Y. He, S. Liu, Y.-H. Zhang, E. A. Kadlec, B. V. Olson, and E. A. Shaner, Appl. Phys. Lett. **106**, 071107 (2015).
[39] A. Zussman, B. F. Levine, J. M. Kuo, and J. de Jong, J. Appl. Phys. **70**, 5101–5107 (1991).
[40] W. E. Tennant, D. Lee, M. Zandian, E. Piquette, and M. Carmody, J. Electron. Mater. **37**, 1406–1410 (2008).
[41] D. Z. Ting, A. Soibel, A. Khoshakhlagh, S. B. Rafol, S. A. Keo, L. Höglund, A. M. Fisher, E. M. Luong, and S. D. Gunapala, Appl. Phys. Lett. **113**, 021101 (2018).
[42] J. Kim, H. Yuan, J. Kimchi, J. Lei, E. Rangel, P. Dreiske, and A. Ikhlassi, Proc. SPIE **10624**, 108–115 (2018).